ACS APPLIED MATERIALS & INTERFACES

Research Article

www.acsami.org

Synthesis of Multifunctional Fe_3O_4–CdSe/ZnS Nanoclusters Coated with Lipid A toward Dendritic Cell-Based Immunotherapy

Jinhoo Jeong,[†,‡] Eun-Kyung Kwon,[§,‡] Taek-Chin Cheong,[§] Heeyeon Park,[†] Nam-Hyuk Cho,*[,§] and Woong Kim*[,†]

[†]Department of Materials Science and Engineering, Korea University, Seoul 136-713, Republic of Korea

[§]Department of Microbiology and Immunology, Seoul National University College of Medicine, and Institute of Endemic Disease, Seoul National University Medical Research Center and Bundang Hospital, Seoul 110-799, Republic of Korea

Supporting Information

ABSTRACT: We demonstrate a novel route to synthesize Fe_3O_4–CdSe/ZnS multifunctional nanoclusters (MNCs) with excellent optical and magnetic properties and biocompatibility. The successful fabrication of highly fluorescent and magnetic MNCs is achieved via a coupling process based on a partial ligand exchange reaction at the aqueous–organic solution interface. In addition, we show that dendritic cells (DCs), the sentinel of the immune system, can uptake the MNCs without significant change in cell viability. The MNCs uptaken by the DCs can be used for imaging, tracking, and separating the DCs. Furthermore, the MNCs can be loaded with a pathogen-associated molecular pattern, lipid A, via a hydrophobic–hydrophobic interaction. Ex vivo labeling of DCs with the MNC–lipid A complex enhances the DC migration to draining lymph nodes and tumor antigen-specific T cell responses in vivo. Our work may contribute to the development of synthetic routes to various multifunctional nanoclusters and DC-based cancer immunotherapies.

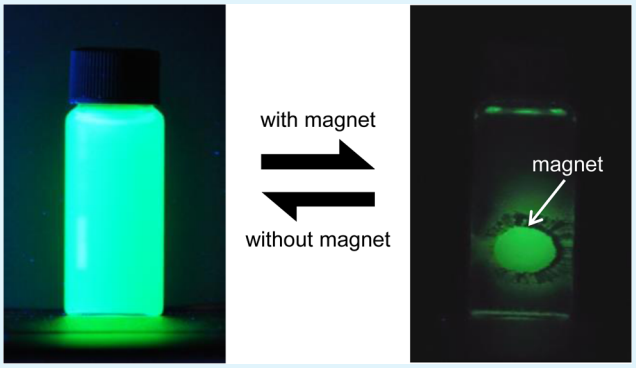

KEYWORDS: *multifunctional, nanocluster, fluorescent, superparamagnetic, dendritic cell, T cell, immunotherapy*

INTRODUCTION

Development of submicrometer particles featuring multiple characteristics such as magnetization, fluorescence, and biological activity is highly desirable for biomedical diagnosis and therapy.[1,2] Most biotechnological processes needed in both diagnosis and therapy often involve various steps such as imaging, tracking, and separating biological molecules and/or cells. The development of a multifunctional nanomaterial that can be used for these various steps may contribute to making the processes more efficient and simpler for diverse therapies including cancer treatment.[3,4]

Immunotherapy is an emerging category of cancer treatment, and the dendritic cell (DC)-based approach is considered as one of the most promising cancer immunotherapies because DCs play a central role in immune system.[5,6] Recently, DCs have been utilized as potent therapeutic vaccines against human cancers.[7−10] In DC vaccine trials, most efforts are focused on generating a large number of cytotoxic effector T cells in vivo and overcoming the immunosuppressive tumor environment. To improve the efficacy of DC vaccination, diverse strategies have been developed such as generation of specific DC subsets, selection of tumor-associated antigens, efficient antigen loading, and efficacious delivery of DC to regional lymph nodes.[7,10,11] Especially, it is essential to effectively track DCs to the lymph nodes of the patient, because the DC must migrate into lymphoid tissues and interact with antigen-specific T cells to induce immune responses. Thus far, several noninvasive imaging techniques for the DC tracking have been reported, which include scintigraphy, bioluminescence, single positron emission tomography, and magnetic resonance imaging (MRI).[12−15] Among them, MRI using superparamagnetic iron oxide nanostructures offers exceptional contrast for soft tissues such as secondary lymphoid tissues and can provide in vivo images with high resolution and signal-to-noise ratios.[9,16]

The DC immunotherapy may be benefited greatly from the advanced multifunctional nanomaterials. Fluorescent and magnetic properties of the nanomaterials can be used for effective and noninvasive tracking of DCs based on optical detection and MRI. In addition, high magnetization of nanomaterials may also be useful for separating and concentrating DCs. Moreover, nanomaterial-assisted delivery of molecular adjuvants such as lipopolysaccharide, CpG oligonucleotides, and antigens may contribute to enhancing anticancer immunity.[9,17] Therefore, an approach based on

Received: January 31, 2014
Accepted: March 18, 2014
Published: March 18, 2014

multifunctional nanomaterials may become a valuable tool to promote immune responses against cancers, simplify ex vivo manipulation steps of the immune cells, and enhance the efficacy of cancer immunotherapy.

However, development of multifunctional nanomaterials requires a careful design strategy and accurate methodology, because there is a trade-off between the multiple functionalities and the complexity arising from multiple synthetic steps.[18] The preparation methods of the multifunctional nanomaterials can be categorized into three types according to Wang et al., including a coupling method, inorganic synthesis, and an encapsulation method.[3] It is simple to prepare fluorescent and magnetic composite nanomaterials via a coupling method through covalent bond linkage or electrostatic attraction between different nanoparticles.[3] Nevertheless, the coupled multifunctional nanomaterials usually suffer from either the loss of fluorescence and low coupling efficiency or the tendency to disintegrate under different analytical conditions. The degradation of fluorescence quantum yield (QY) is ascribed mainly to the loss of the ligands on the surface of quantum dots.[19] Due to this loss, reports on successful coupling between fluorescent quantum dots and magnetic nanomaterials is very rare. Yin et al. recently demonstrated an indirect coupling of Fe_3O_4 nanoclusters and quantum dots by using a silica layer between the two components.[19]

Another route to prepare the multifunctional nanoparticles is the direct chemical synthesis of fluorescent quantum dots on magnetic cores.[20,21] However, only specific combinations are usually available because the growth of the fluorescent nanomaterials is highly dependent on the magnetic core materials. Moreover, the composite nanomaterials prepared by this synthetic method also have low QY and hence are difficult to use directly in biological applications. Finally, different kinds of nanoparticles can be encapsulated in a matrix material such as polymers and silica for multifunctionality. This encapsulation method is highly valued and has a great potential for medical applications. Nonetheless, magnetic or optical properties of multifunctional nanoparticles could be further enhanced if the matrix materials, which are neither fluorescent nor magnetic, are eliminated.

In this work, we demonstrate a novel synthetic route toward multifunctional nanoclusters (MNCs) without using matrix materials. The Fe_3O_4 nanoclusters ($d \sim 200$ nm) were chemically coupled with CdSe/ZnS quantum dots ($d \sim 6$ nm) via a partial ligand exchange reaction. We chose Fe_3O_4 nanoclusters ($d \sim 200$ nm) as a magnetic component of multifunctional nanomaterials, because they have high magnetization value owing to large size and superparamagnetic property arising from the cluster structure.[22,23] For a fluorescent component, we chose CdSe/ZnS semiconducting quantum dots, which are appropriate for proof-of-concept experiments, because they have been extensively studied and have excellent photostability, brightness, and optical tunability that traditional organic dyes may not have.[24−26] The partial ligand exchange reaction enabled the fabrication of the MNCs with high fluorescence QY, magnetization, integrity, and water dispersibility that are desirable properties for biomedical applications. Moreover, we demonstrate their applications for the activation of DCs and the induction of immune responses in mice. The MNCs were loaded with bioactive materials such as lipid A via a simple hydrophobic−hydrophobic interaction. Ex vivo labeling of DCs with the MNC−lipid A complexes enables us to measure the loading efficacy of the complexes by flow cytometry and detect the cells by magnetic resonance scanner without significantly affecting viability. Finally, we show that co-delivered lipid A can mediate efficient activation and in vivo migration of DCs into draining lymph nodes, which ultimately enhances tumor antigen-specific T cell responses in vivo.

RESULTS AND DISCUSSION

Synthesis and Characterization of Fe_3O_4 Core Nanoclusters. We prepared a core of superparamagnetic Fe_3O_4 nanoclusters with superparamagnetism and high magnetization. These are desirable properties when nanoclusters are used in biological procedures for efficient cell separation, magnetic imaging, and water dispersibility.[22,23] High magnetization was achieved by using relatively large magnetic nanoclusters; the diameter of the nanoclusters was in the range of 200 to 400 nm (Figure 1a,b). Larger particles have higher magnetization and hence can lead to more efficient cell separation,[22,27] but one cannot simply increase the size of Fe_3O_4 particles because a transition occurs from superparamagnetism to ferromagnetism at the size of approximately 20−30 nm.[28] Due to the ferromagnetism, the large Fe_3O_4 particles will be aggregated and not be easily redispersed even when magnetic field is removed. Therefore, we chose to prepare a nanocluster

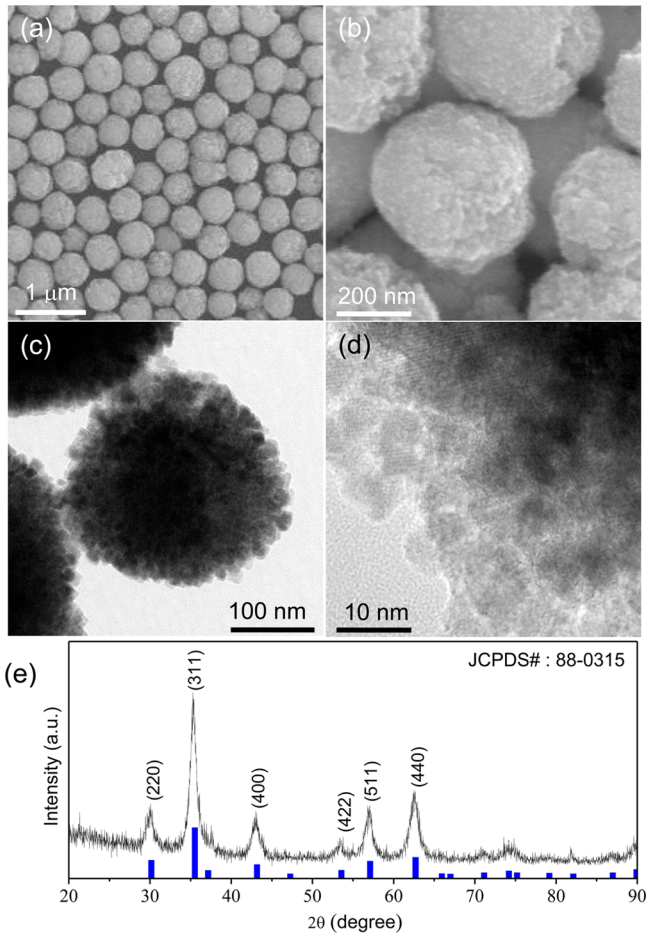

Figure 1. (a), (b) SEM images and (c) TEM image of Fe_3O_4 nanoclusters. (d) TEM of individual Fe_3O_4 nanoparticles comprising a nanocluster. (e) X-ray diffraction (XRD) pattern of Fe_3O_4 nanoclusters and comparison with the reference JCPDS no.88-0315.

composed of small superparamagnetic Fe_3O_4 nanoparticles (Figure 1c,d). The individual Fe_3O_4 nanoparticles are sufficiently small (d = 5 ~ 10 nm) so that the large nanocluster is superparamagnetic and also has high magnetization. Transmission electron microscopy (TEM) and X-ray diffraction measurement (XRD) analysis confirms that each nanoparticle is highly crystalline (Figure 1d,e). The diameter of the Fe_3O_4 nanoparticles (d ~ 6.4 nm) estimated from the XRD data and Scherrer formula is consistent with the TEM results.[29] The large water dispersible superparamagnetic nanoclusters are useful for efficient separation and concentration of cells and MRI.

Synthesis and Characterization of CdSe/ZnS Quantum Dots. We prepared CdSe/ZnS quantum dots which were highly fluorescent. The nanocrystals show QY of >80% which can be attributed to the graded chemical composition across the core−shell interface.[24] The quantum dots are approximately 6 nm in diameter (Figure 2a) and crystalline, as indicated by TEM images and selected area electron diffraction (SAED) pattern (Figure 2b,c). Energy-dispersive X-ray spectroscopy (EDX) shows that the composition ratio of Cd/Se/Zn/S is approximately 1:1:9:9. The absorption and photoluminescence spectrum (λ_{max} ~ 530 nm) are shown in Figure 2d. Inset shows photographs of a vial containing the quantum dots dispersed in toluene. There is a tint of green fluorescence even under room light. Strong green fluorescence can be seen in the darkness upon illumination of UV (λ ~ 365 nm).

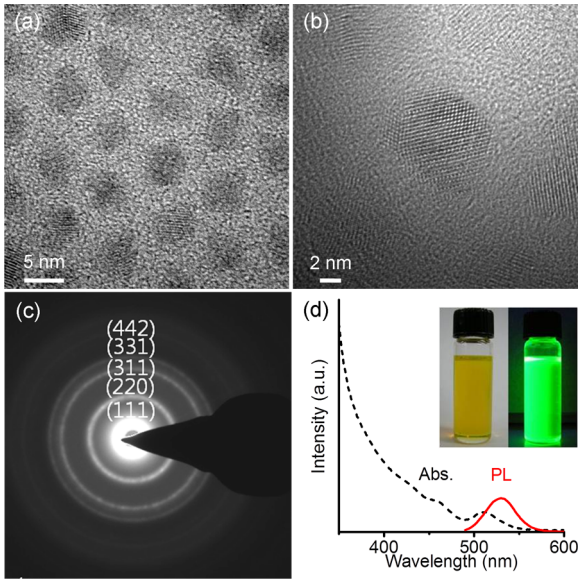

Figure 2. (a), (b) TEM images of CdSe/ZnS nanocrystals. (c) Selected area electron diffraction pattern of the CdSe/ZnS nanocrystals. (d) UV−vis absorption (black dash line) and photoluminescence (red line, λ_{ex} = 480 nm) spectra of CdSe/ZnS quantum dots. Inset: the photographs taken under room light and UV light (excited by a hand-held UV lamp, λ_{ex} = 365 nm).

Conjugation of Fe_3O_4 Core Clusters and CdSe/ZnS Quantum Dots. The conjugation of the core clusters and the quantum dots were successfully carried out using an *N*-(3-dimethylaminopropyl)-*N*′-ethylcarbodiimide hydrochloride (EDC)/ *N*-hydroxysulfosuccinimide sodium salt (sulfo-NHS) coupling and a ligand exchange reaction. A schematic illustrates the conjugation procedure (Figure 3). First, the surface of core nanoclusters is functionalized with thiol groups via the EDC/NHS coupling reaction.[30] Next, the thiols on the core clusters partially replace existing ligands of CdSe/ZnS. We used thiol groups because they are known to have strong affinity to CdSe/ZnS surface.[31] The conjugation reaction occurred at the interface between aqueous and organic solution containing the hydrophilic Fe_3O_4 nanoclusters and the hydrophobic CdSe/ZnS nanoparticles, respectively. Once they were conjugated, the resulting MNCs were localized at the aqueous/organic interface. Moreover, we confirmed that thiol goups on the Fe_3O_4 indeed played a essential role in the conjugation process. Without the thiol groups, the conjugation did not occur, and the CdSe/ZnS nanoparticles and the Fe_3O_4 nanoclusters remained in their original solutions (Supporting Information, Figure S1).

This partial-ligand-exchange approach was the key to the successful coupling of fluorescent and magnetic MNCs, which has rarely been demonstrated before this work. A generally practiced coupling process involves an extensive ligand exchange reaction to provide quantum dots with hydrophilicity for water dispersibility; the hydrophobic ligands on the quantum dots used in the synthesis are replaced with hydrophilic ligands.[7] However, this replacement is often not complete, and the loss of original ligands leads to insufficient passivation of quantum dots. As a result, fluorescence efficiency becomes unacceptably low, and the quantum dots aggregate.[19,32]

The quantum dots prepared in our work are sufficiently fluorescent even after the conjugation and subsequent chemical

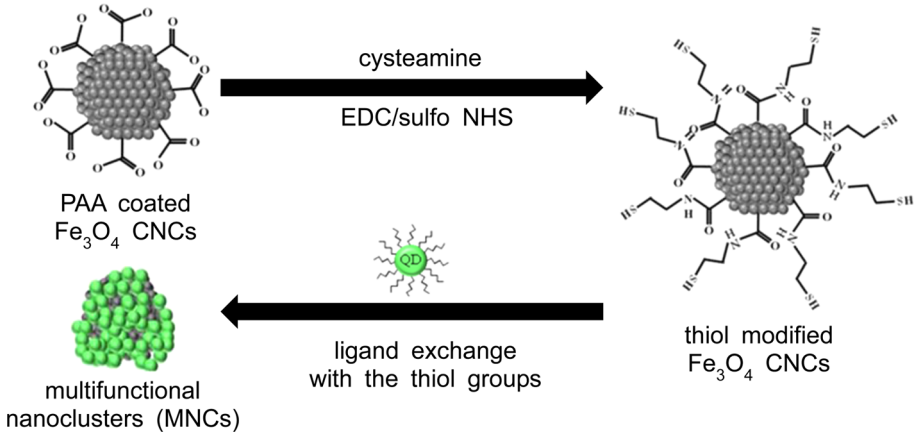

Figure 3. Schematic diagram of the conjugation process between Fe_3O_4 colloidal nanoclusters (CNCs) and quantum dots.

dx.doi.org/10.1021/am500661j | ACS Appl. Mater. Interfaces 2014, 6, 5297−5307

and biological processes. This is because only a small portion of the quantum dot ligands are replaced, and a majority of them may have remained on the surface of the quantum dots. This was possible because we used the ligands anchored on the large Fe_3O_4 core clusters to replace the ligands on the CdSe/ZnS quantum dots. The access of the ligands on the large Fe_3O_4 particles to the ligands on the small CdSe/ZnS particles is sterically hindered, and hence, only the minimum number of the quantum-dot ligands can be replaced.[19] In addition, the ligand exchange step was the last step of the MNC preparation, and no further steps were necessary, which may degrade the passivation. Apparently, the MNCs were hydrophilic and dispersible in water. We observed over 6 months that the MNCs could stably be stored in DI water without noticeable property degradation. However, the MNCs also have local surface area with hydrophobic properties, especially where the hydrophobic CdSe/ZnS nanoparticles are conjugated. The hydrophobic functional groups of MNCs were used to load bioactive materials via a hydrophobic interaction in the following step.

Electron Microscopic Characterization of the MNCs. We confirmed that the CdSe/ZnS nanoparticles were uniformly coated on the Fe_3O_4 clusters by analyzing various characteristics. Scanning electron microscopy (SEM) images of the Fe_3O_4−CdSe/ZnS core−shell nanoclusters show that the shape of the nanoclusters was generally unchanged after the conjugation process without noticeable aggregation of quantum dots (Figure 4a,b). This implies that the CdSe/ZnS nanoparticles were uniformly coated. TEM images and corresponding SAED on the edges of clusters confirm the presence of CdSe/ZnS quantum dots on the magnetic clusters. Fe_3O_4 and CdSe/ZnS nanoparticles were identified using inverse fast Fourier transform (FFT) and masking technique.[33,34] They are marked with green-solid and red-dotted circles, respectively (Figure 4c,d). EDX mapping shows that Zn and S are homogeneously distributed over the whole Fe_3O_4 core nanocluster (Figure 4e). The results also indicate that CdSe/ZnS quantum dots are uniformly conjugated on the surface of core nanoclusters. The integrity of the conjugated nanoclusters was excellent. The MNCs were exposed to various characterization and application environments without any significant change in material properties.

Surface Properties of the Nanoclusters. Functionalization or conjugation at each step of the coupling process was confirmed by Fourier transform infrared spectroscopy (FT-IR) spectroscopy (Figure 5a). The spectrum of poly(acrylic acid) (PAA)-coated Fe_3O_4 nanoclusters indicates the presence of large amounts of carboxylate groups. The peak at 1715 cm^{-1} corresponds to the stretching mode of carbonyl bond in protonated carboxylate groups. Two peaks located at 1536 and 1411 cm^{-1} correspond to asymmetric and symmetric C−O stretching mode of carboxylate groups coordinated to the iron cations, respectively.[35] Thiol functionalization by EDC/sulfo-NHS coupling between the PAA-coated Fe_3O_4 nanoclusters with cysteamine was verified by the presence of peak at 1618 cm^{-1} as reported elsewhere.[36,37] Conjugation with CdSe/ZnS led to the appearance of peak at 1626 cm^{-1} corresponding to the carboxylate of oleic acid anchored onto the surface of the quantum dots.[38,39] Finally, lipid-A coatings on the MNCs were confirmed by the P−O−C stretch peak of phosphate located 985 cm^{-1}.[40] In addition, we show the zeta potentials of the products collected at each step of the conjugation process (Figure 5b). The zeta potential of the PAA-coated Fe_3O_4 was

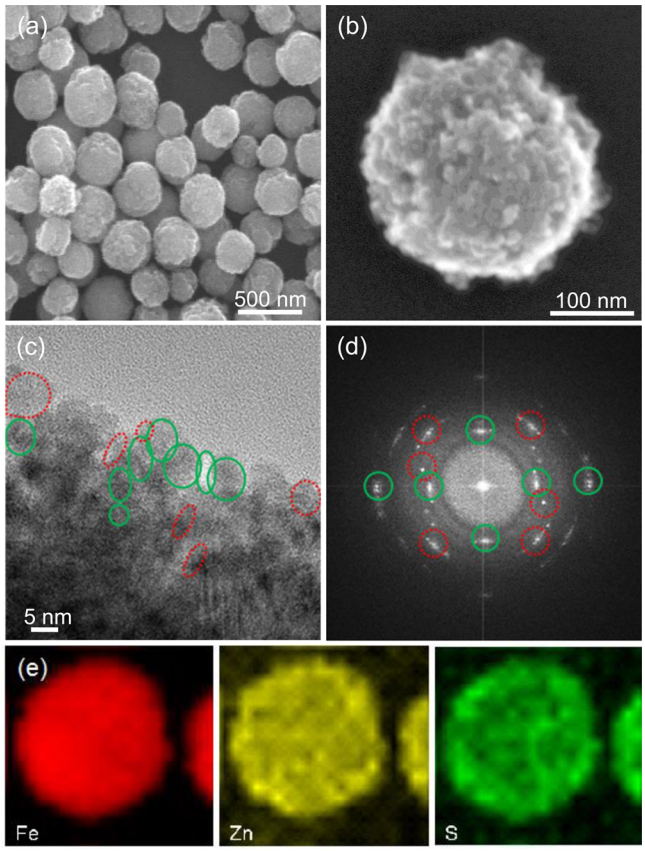

Figure 4. (a), (b) SEM images and (c) TEM image of Fe_3O_4−CdSe/ZnS MNCs. Red-dotted and green-solid circles correspond to Fe_3O_4 nanoparticles and CdSe/ZnS quantum dots, respectively. (d) Fast Fourier transform (FFT) image of (c). (e) EDX mapping data for Fe, Zn, and S.

−31.4 mV indicating that these particles have decent dispersion stability. The high dispersibility can be attributed to the high proportion of PAA in a Fe_3O_4 nanocluster. Thermogravimetric analysis (TGA) indicates that percentage of the PAA is ∼16.3 wt% (Supporting Information, Figure S2). Upon thiol functionalization, some carboxylic acid groups are modified with cysteamine to present thiol groups on the surface of the Fe_3O_4 clusters leading to the reduction of absolute value of negative zeta potential. Successive coupling with hydrophobic quantum dots further reduced the value to −21.9 mV. Finally, coating of the lipid A on the MNCs increased the absolute value of the zeta potential (ζ = −27.2 mV). This is because the negatively charged hydrophilic side of the lipid A is exposed on the surface of the MNCs while the other side of the lipid A is anchored on the hydrophobic ligands of the quantum dots.

Fluorescent and Magnetic Properties of the MNCs. We verified that the prepared MNCs indeed have both fluorescent and superparamagnetic properties. Confocal microscopy clearly indicates that most of individual Fe_3O_4−CdSe/ZnS clusters are fluorescent. The left panel in Figure 6a shows a differential interference contrast image of individual nanoclusters. Corresponding fluorescence images are shown in the center panel. Overlay of the two images clearly shows that the fluorescence comes from individual nanoclusters. On the other hand, the nanoclusters have superparamagnetic properties before and after the conjugation as shown in the magnetization (M−H) curve (Figure 6b). No hysteresis indicates that the magnetic nanoclusters are not ferromagnetic but super-

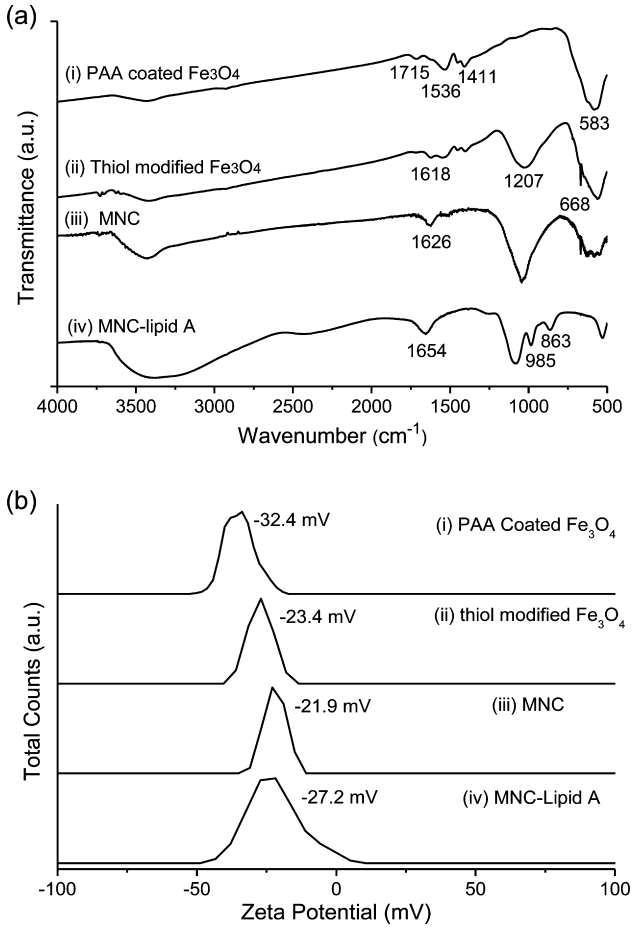

Figure 5. (a) FT-IR spectra and (b) zeta potentials of (i) PAA-coated Fe_3O_4 nanoclusters, (ii) thiol-modified Fe_3O_4 nanoclusters, (iii) Fe_3O_4–CdSe/ZnS MNCs, and (iv) lipid-A-coated MNCs.

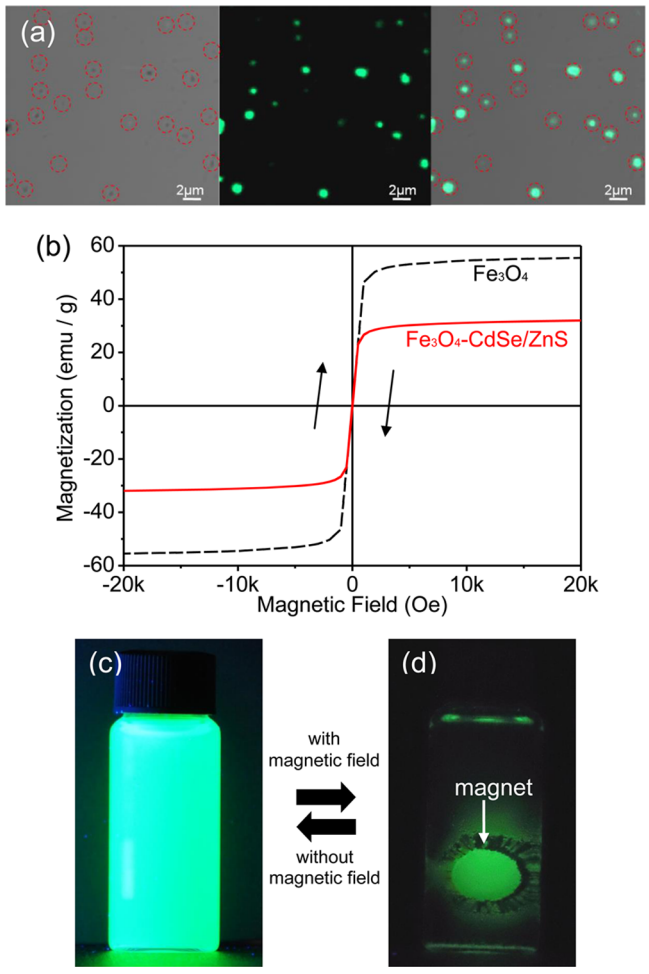

Figure 6. (a) Confocal laser scanning microscopy image of MNCs. Red circles indicate luminescent Fe_3O_4–CdSe/ZnS nanoclusters. (b) Magnetization curves of Fe_3O_4 nanoclusters (black dash line) and Fe_3O_4–CdSe/ZnS nanoclusters (red line). Photographs of Fe_3O_4–CdSe/ZnS nanoclusters (c) dispersed in deionized water and (d) collected by a permanent magnet (excited by a hand-held UV lamp, λ_{ex} = 365 nm).

paramagnetic. Saturation magnetization of Fe_3O_4 core nanoclusters and Fe_3O_4–CdSe/ZnS core–shell nanoclusters are ~55.5 and ~31.9 emu/g, respectively. The saturation magnetization was reduced to approximately two-thirds after the conjugation. However, it is sufficiently high to be used for both imaging and cell separation. Magnetization per grain and cluster were 2.47×10^{-16} and 2.50×10^{-11} emu, respectively. The values were estimated by fitting the M–H data measured by vibrating sample magnetometer (VSM) into Langevin function, assuming that the sizes of grains and clusters are 6.43 and 300 nm, respectively (Supporting Information, Figure S3).[22]

Furthermore, we demonstrate that the MNCs have both superparamagnetic and fluorescent properties at the same time (Figure 6c,d). Fe_3O_4–CdSe/ZnS nanoclusters dispersed in DI water were highly fluorescent under UV illumination, as shown in Figure 6c. When neodymium (NdFeB) permanent magnet (cylindrical shape, $d \sim 1$ cm and $L \sim 1.5$ cm) was placed in the back side of the vial, within a minute, the nanoclusters accumulated where the magnet was positioned (Figure 6d). This quick response can be attributed to high magnetization of large nanoclusters. We placed the magnet about 1 cm above the bottom to show that the accumulation is not due to the gravity and sedimentation. Disappearance of fluorescence in solution upon MNC accumulation clearly shows that the fluorescence indeed comes from the superparamagnetic MNCs. This process is reversible; removal of the magnetic field and brief stirring led to uniform redispersion of the nanoclusters in the solution. A real-time movie of the collection and redispersion process is provided (Supporting Video S1).

Intracellular Delivery of MNCs into DCs. We observed that the MNCs were engulfed by DCs. DCs were prepared from mice as described previously[9] and loaded with MNCs. Immature DCs were incubated with different concentrations of MNCs for 18 h, and then cellular uptake was measured by confocal microscopy and flow cytometry (Figure 7a). The intracellular delivery of MNCs into DCs was gradually increased in a concentration-dependent manner and saturated at the concentration of ~500 μg/mL. More than 50% of DCs took up substantial amounts of MNCs at the saturating condition. The intracellular MNCs were dispersed throughout the cytoplasm and were found in aggregated forms (inset in Figure 7a), and they may have been taken up via phagocytosis.[41] The MNC-loaded DCs were efficiently separated and enriched by magnetic separation (Supporting Information Figure S4), potentially due to high magnetization of MNCs. Separation and enrichment of the labeled cells might be useful to enhance the fluorescent and superparamagnetic signals to tracing the cells in vivo.

dx.doi.org/10.1021/am500661j | ACS Appl. Mater. Interfaces 2014, 6, 5297–5307

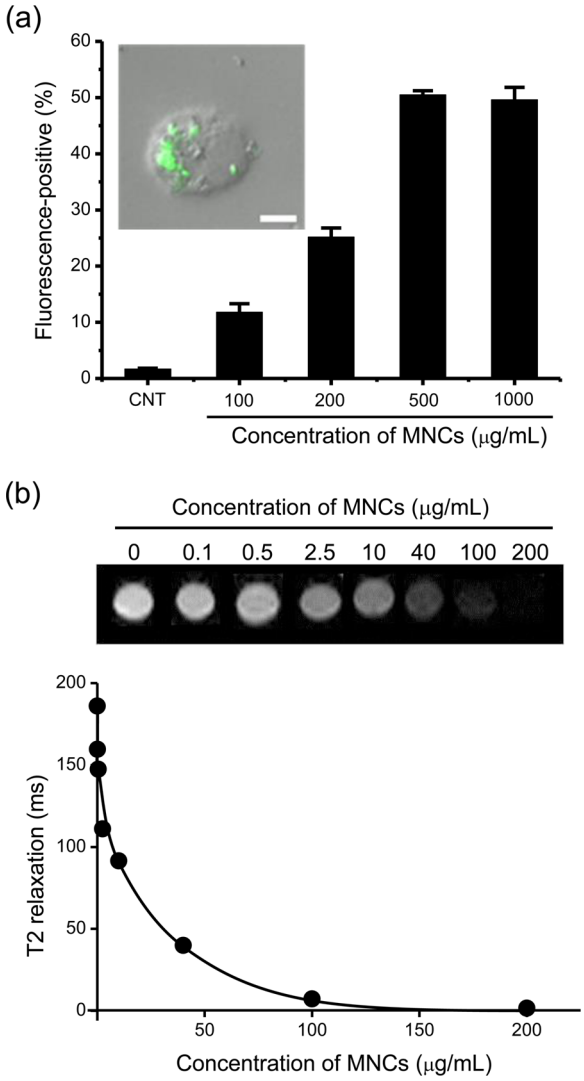

Figure 7. (a) Degree of MNC uptake by dendritic cells (DCs) at various MNC concentrations, quantified by FACS. (b) MRI and T2 relaxation time of DCs loaded with MNCs at various concentrations.

Viability of MNC-Loaded DCs and MRI. DCs incubated with variable concentrations of MNCs (100−500 μg/mL) showed no significant changes in viability for 7 days (Supporting Information Figure S5). The maturation markers of the DCs were examined before and after loading with MNCs, and interestingly, the surface expression of the maturation markers (CD40, CD80, and CD86) on the DCs was not significantly affected by the MNC loading (Supporting Information Figure S6). In addition, we demonstrate that the intracellular MNCs may be used for MRI. DCs loaded with different concentrations of MNCs were applied for in vitro MRI experiments, and we show MRI of the DCs revealed that the T2 relaxation time is gradually reduced (image was darkened), with maximum saturation at the MNC concentration of ~200 μg/mL after 18 h of incubation (Figure 7b). This demonstrates that MNCs can be applied for noninvasive MRI-guided monitoring of DCs.

Activation of DCs with Lipid-A-Coated MNCs. We demonstrate that the pathogen-associated molecular pattern can be simply incorporated onto the MNCs via hydrophobic interaction. These MNC−lipid A complexes could boost DC-mediated immune responses.[42] We chose a lipophilic monophosphoryl lipid A because this bacteria-derived lipid A molecule has been extensively used as a potent stimulator for DC activation and widely applied to manufacture "pathogen-mimetic" nanostructures.[43,44] Lipid A molecules were readily incorporated to the MNCs and the complex formation was confirmed by confocal microscopy after immunofluorescent staining (Figure 8a). Approximately 0.8 ng of lipid A was attached to 1 μg of MNCs, and this corresponds to ~2×10^4 lipid A molecules per MNC. The MNC−lipid A complexes were stable even after being taken up by DCs (Figure 8b). To examine whether the complexes can induce DC activation, we incubated DCs with the MNC−lipid A complexes in the culture media and measured the surface expression of activation markers at 18 h after the incubation (Figure 8c). The complexes enhanced surface expression of the activation markers as efficiently as free lipid A, in contrast to uncoated MNCs which barely induced DC maturation. In addition, fluorescently labeled DCs stimulated with the MNC−lipid A complexes showed enhanced migration in vivo from the footpads of mice to the draining lymph nodes at 2 days after injection (Figure 8d). The MNC−lipid A induced DC migration more than two times compared to control (CNT) groups. A schematic of lipid A coating process on the MNC surface is shown in Figure 8e.

Induction of Antigen-Specific T Cell Responses. Finally, we demonstrate that DCs stimulated with MNC−lipid A complexes can significantly induce the antigen-specific T cell responses in both draining lymph node and spleen of mice. Mice were immunized with DCs, which were stimulated with the indicated agent and loaded with carcinoembryonic antigen (CEA)-derived T cells epitopes. CEA-specific cellular immunity was analyzed in the draining lymph nodes and spleen by measuring production of IFN-γ, a hallmark cytokine for cell-mediated immunity, at 7 days after DC immunization twice at weekly intervals. Significant induction of T cell responses were observed in both the draining lymph node and spleen (Figure 9 and Supporting Information Figure S7 and S8). The frequency of IFN-γ-secreting T cells was approximately 6-fold higher in the lymphoid organs of mice immunized with lipid A- or MNC−lipid A-loaded DCs than immature (control) or MNC-loaded DCs. This result suggests that DC activation and migration induced by MNC−lipid A can ultimately contribute to enhanced T cell immunity in vivo.

CONCLUSION

We developed a new technology for manufacturing MNCs with excellent optical and magnetic properties and biocompatibility. The MNCs were prepared by conjugating superparamagnetic Fe_3O_4 nanoclusters with highly fluorescent CdSe/ZnS nanoparticles via a partial ligand exchange at the aqueous−organic solution interface. The MNCs loaded in DCs enabled us to monitor the DCs using conventional fluorescence microscopy and magnetic resonance detector without significant changes in cellular viability. In addition, the MNC-loaded DCs were efficiently separated and enriched by magnetic separation possibly owing to high magnetization of the MNCs. Moreover, we demonstrate that the MNCs can efficiently form a complex with lipid A molecules via a simple incubation in a cell culture media. Finally, we observed that the MNC-lipid A complexes enhanced the maturation of DCs, their in vivo migration into draining lymph nodes, and the induction of antigen-specific T cell responses. Our work may contribute to developing novel approaches to deliver vaccines, to enhance specific immunity

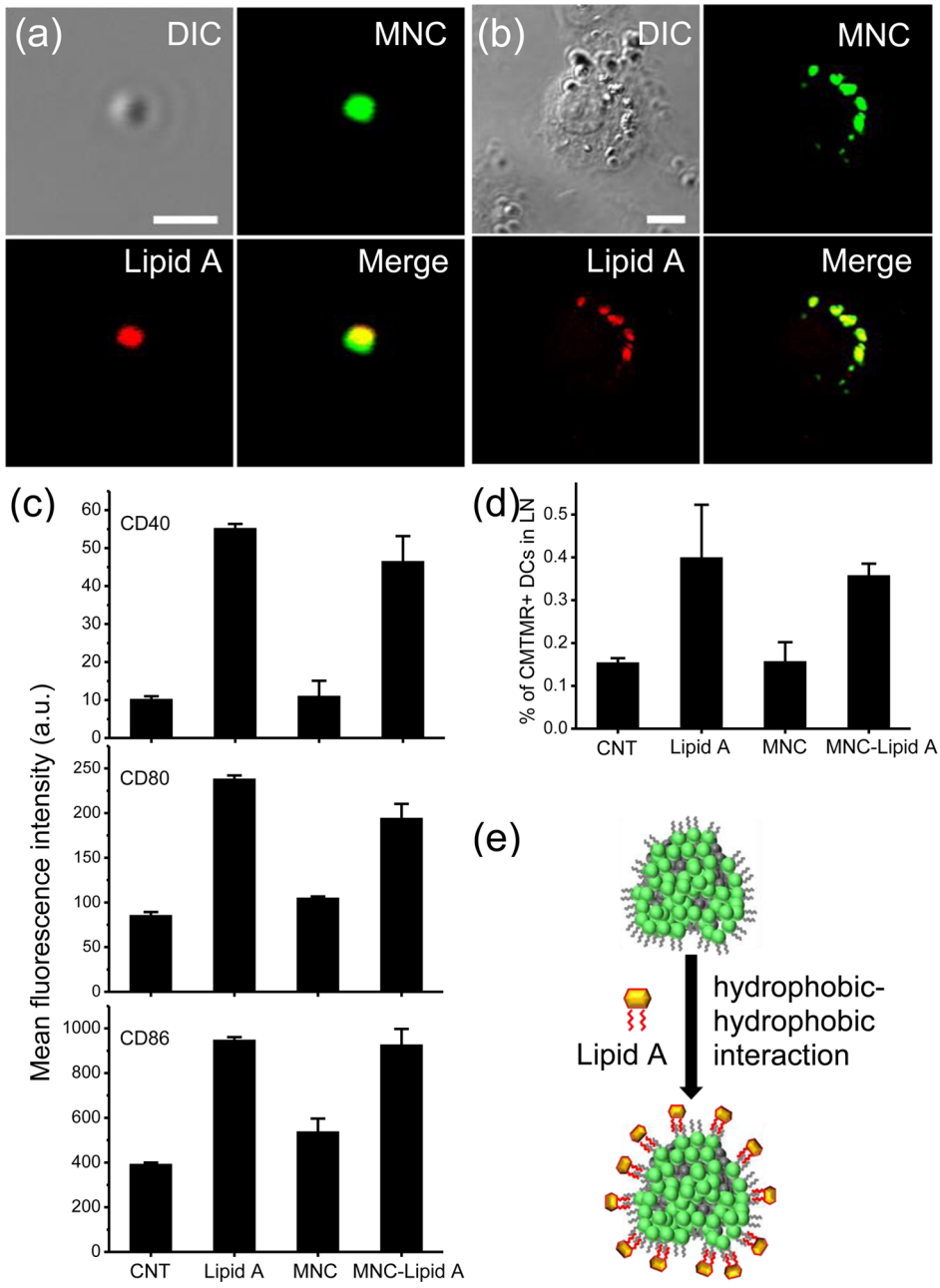

Figure 8. Confocal microscopy image of (a) lipid-A-coated MNC and (b) MNC−lipid A complexes uptake by a DC. (c) Expression of CD40, CD80, and CD86 of DCs stimulated with lipid A, MNC, and MNC−lipid A. Control data is included. (d) Degree of DC migration to lymph node that are stimulated with lipid A, MNC, and MNC-lipid A. (e) Lipid A coating process on a MNC via a hydrophobic interaction.

against malignant cancers and finally to enhance clinical efficacy for DC-based cancer immunotherapies.

■ MATERIALS AND METHODS

Materials for Fe_3O_4 and CdSe/ZnS Synthesis. All chemicals were used as received without further purification. Cadmium oxide (≥99.99%), zinc acetate (99.99%), selenium (Se) powder (99.99%), elemental sulfur (S, 99.998%), iron(III) chloride hexahydrate ($FeCl_3{\cdot}6H_2O$, 97%), poly(acrylic acid) (PAA, average M_w ~1,800), sodium acetate (≥99.0%), *N*-(3-dimethylaminopropyl)-*N*′-ethylcarbodiimide hydrochloride (EDC, BioXtra), *N*-hydroxysulfosuccinimide sodium salt (sulfo-NHS, ≥98.5%), cysteamine (~95%), oleic acid (≥99%), 1-octadecene (90%), trioctylphosphine (90%), 1-octanethiol (98.5+%), ethylene glycol (99.8%), toluene (99.8%), and phosphate-buffered saline (PBS, 1.0 M, pH 7.4) were purchased from Sigma-Aldrich. Absolute ethanol (99.9%) was purchased from J. T. Baker.

Synthesis of Fe_3O_4 Nanoclusters. We prepared the nanoclusters using hydrothermal method by slightly modifying a previously reported procedure.[22,45,46] First, $FeCl_3{\cdot}6H_2O$ (0.675 g, 2.5 mmol) was completely dissolved in ethylene glycol (25 mL) by sonication for 5 min, which led to a clear orange solution. Second, PAA (0.72 g) and sodium acetate (2.16 g) were added to the solution. The mixture was stirred vigorously for 20 min and then sealed in a Teflon-lined stainless-steel autoclave (inner volume = 35 mL). Finally, the autoclave was heated at 220−240 °C for 4 h. After the reaction,

dx.doi.org/10.1021/am500661j | ACS Appl. Mater. Interfaces 2014, 6, 5297−5307

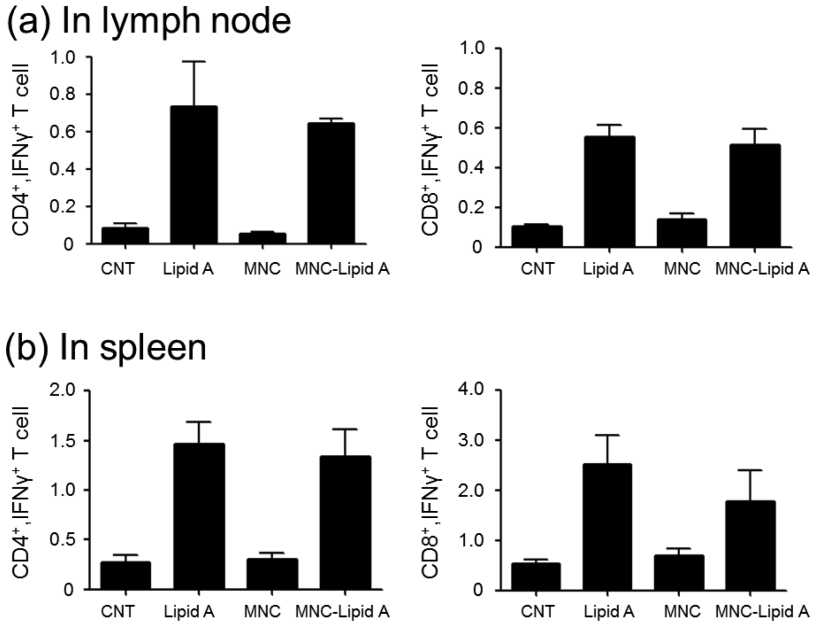

Figure 9. Induction of CEA-specific T cell immunity by MNC-loaded DCs; the frequency of $CD4^+$, INF-γ^+ T-cells and $CD8^+$, INF-γ^+ T-cells obtained from (a) lymph node and (b) spleen. Injected dendritic cells were immature (control) or stimulated with lipid A, MNC, and MNC−lipid A.

the autoclave was naturally cooled to room temperature. After adding ethanol (15 mL) to the solution, the Fe_3O_4 nanoclusters were precipitated either by centrifugation or by using a magnet. Supernatant containing any unreacted precursors was removed. The Fe_3O_4 nanoclusters were redispersed in deionized (DI) water (30 mL). This washing step was repeated until the supernatant became clear. The Fe_3O_4 nanoclusters were redispersed in 30 mL of PBS solution for further use.

Synthesis of CdSe/ZnS Core/Shell Nanoparticles. We chemically synthesized the CdSe/ZnS nanoparticles according to Lee's method.[24] Cadmium oxide (13 mg, 0.1 mmol) and zinc acetate (732 mg, 4 mmol) were added to oleic acid (5 mL) in a 100 mL three-neck flask. The solution was heated at 150 °C for approximately 30 min under N_2 atmosphere until the solution became clear. 1-Octadecene (15 mL) was injected into the reaction flask and heated to 300 °C. Then, Se powder (16 mg, 0.2 mmol) and elemental S (96 mg, 3.0 mmol) dissolved in trioctylphosphine (2 mL), were swiftly injected into the reaction mixture. The temperature was held at 300 °C for 8 min. After the reaction, 1-octanethiol (0.5 mL) was injected into the solution to passivate the surface of the quantum dots. After the solution cooled to room temperature, the CdSe/ZnS core/shell nanoparticles were washed with ethanol three times and redispersed in toluene (15 mL). The QY of the nanoparticles was estimated by comparing it with that of standard dye solutions (9,10-diphenyl anthracene in cyclohexane, QY = 95%).

Conjugation of a Fe_3O_4 Nanocluster and CdSe/ZnS Quantum Dots. The conjugation was performed by modifying the surface Fe_3O_4 with thiol groups and partially replacing the ligands of the CdSe/ZnS with the thiols. First, the surface of the Fe_3O_4 nanoclusters was functionalized with thiol groups. This was carried out by conjugating the carboxylic acid group of PAA on the Fe_3O_4 nanoclusters and amine group of cysteamine via EDC/sulfo-NHS coupling reaction. More specifically, EDC (0.4 mmol) and sulfo-NHS (0.2 mmol) were added into 5 mL of the PBS containing Fe_3O_4 nanoclusters. After the solution was gently shaken for 30 min at room temperature, cysteamine (1 mmol) was added into the solution. The reaction proceeded for 2 h under the gentle shake. The thiol-modified Fe_3O_4 nanoclusters were washed three times with PBS via magnetic precipitation and decantation. The precipitates were redispersed in PBS solution (10 mL). Next, the Fe_3O_4 nanoclusters were conjugated with quantum dots by exchanging ligands of the quantum dots partially with thiols on the Fe_3O_4 nanoclusters as follows. The quantum dot solution (5 mL) was added to PBS containing the thiol-modified Fe_3O_4 (10 mL). We advise that this reaction occurs at aqueous/organic interface; the hydrophobic quantum dots and hydrophilic magnetic nanoclusters were dispersed in toluene and PBS, respectively. To facilitate this reaction, the solution was magnetically stirred at 80 °C for over 24 h, which led to the formation of fluorescent and magnetic nanoclusters. The fluorescent and magnetic MNCs were separated magnetically and washed three times with a mixture of toluene and DI water. The product was rinsed with pure DI water to remove residual toluene and finally redispersed in DI water. Under the assumption that the Fe_3O_4 nanoclusters ($d \sim 300$ nm) were coated with a monolayer of hexagonally close-packed CdSe/ZnS ($d \sim 6$ nm), the ratio of CdSe/ZnS to Fe_3O_4 was estimated to be ~5.8 wt %. This weight percentage corresponds to the number of 9400 CdSe/ZnS particles per nanocluster. In reality, this number would be lower because our observation suggests that the CdSe/ZnS nanoparticles do not fully cover the whole surface of Fe_3O_4.

Characterization of Materials. The size, structure, and morphology of the nanocrystals and nanoclusters were characterized by field emission transmission electron microscopy (FE-TEM, Tecnai G2 F30) and field emission scanning electron microscopy (FE-SEM, Hitachi S-4300). TEM samples were prepared by drop-casting nanomaterials in DI water on carbon-coated 200 mesh copper grids (Electron Microscopy Sciences). The composition of the nanomaterials was analyzed by EDX built on a FE-TEM. The structure was studied with XRD measurement (Rigaku D/max-2500 V/PC), where Cu Kα line ($\lambda = 0.154$ nm) was used. Absorption and emission spectra

dx.doi.org/10.1021/am500661j | ACS Appl. Mater. Interfaces 2014, 6, 5297−5307

of the quantum dots were measured using a UV−vis spectrophotometer (Varian Cary 50) and fluorescence spectrophotometer (Varian Cary Eclipse). The magnetic properties of the nanoclusters were measured with a superconducting quantum interference device (SQUID) magnetometer (Quantum Design MPMS5) and vibrating sample magnetometer (VSM, Lakeshore 665). The fluorescence images of MNCs were obtained with a confocal laser scanning microscope (CLSM, Carl Zeiss LSM5). Surface functional groups and surface charges of the nanoparticles and nanoclusters were analyzed with FT-IR spectroscopy (Nicolet iS10) and zeta-potential measurement (Malvern, Zetasizer Nano ZS90), respectively. The relative amount of the PAAs coated on Fe_3O_4 nanoclusters was determined by TGA (SETARAM, Inc., S60/51920). The measurement was carried out under air at the heating rate of 10 °C/min.

Mice and Cells. C57BL/10NAGCSnAi-(KO) Rag2 (H-2b) mice (Taconic Farms) and C57BL/6 (H-2b) mice (Orient Bio) were housed and maintained in the specific pathogen-free facility at College of Medicine in Seoul National University (SNU). Animal experiments were performed after the approval by the SNU Institutional Animal Care and Use Committee (IACUC, permission ID: SNU-090805-5). DCs were generated from the bone marrow (BM) of 6- to 12-week-old Rag2 knockout mice.[9] The BM cells were flushed out of the femurs and tibias with serum-free Iscove's modified Dulbecco's medium (IMDM; Gibco Invitrogen). The single cell suspension was then filtered through a nylon cell strainer (70-μm Nylon mesh, BD Biosciences), washed twice with complete IMDM medium supplemented with recombinant mouse granulocyte−macrophage colony-stimulating factor (GM-CSF, 1.5 ng/mL; PeproTech) and mouse interleukin-4 (IL-4, 1.5 ng/mL; PeproTech), penicillin (100 units/ml), streptomycin (100 μg/mL), gentamicin (50 μg/mL), L-glutamine (2 mM), and β-mercaptoethanol (50 nM; Gibco Invitrogen). The cells were seeded in a 24-well plate, where each well contains a final volume of 2 mL of the complete IMDM. The cell concentration per well is ca.1 × 10^6 cells/ml. Half of the medium was replaced every other day with an equal volume of complete IMDM for 6 days.

Intracellular Delivery of MNCs and Confocal Microscopy. For the intracellular delivery of MNCs to BM-derived immature DCs, MNCs were concentrated by a magnetic particle concentrator (Invitrogen Dynal MPC-L) and washed with complete IMDM media. Immature DCs (1 × 10^6 cells), cultured in IMDM medium containing GM-CSF and IL-4 for 6 days, were incubated with MNCs at 37 °C. DCs were then washed with IMDM three times to remove free MNCs. To examine the uptake of MNCs by DCs, cells were transferred onto poly-L-lysine-coated microscope slides (Thermo Scientific), fixed in 4% paraformaldehyde solution for 20 min, and analyzed using a laser scanning confocal microscope (Olympus FV1000). All images were analyzed and processed using the Olympus Fluoview software programs. To make complexes of MNCs with lipid A, 100 μg/mL MNCs were washed twice in PBS and incubated with 100 ng/mL of lipid A (Sigma Aldrich) for 1 h at room temperature. The MNC−lipid A complexes were recovered by magnetic separation and washed with PBS three times. The amount of MNC-bound lipid A was assayed using Limulus Amebocyte Lysate assay kit (Lonza) according to the manufacturer's instruction. Lipid A (0.8 ng) was bound to 1 mg of MNCs (~ 2 × 10^4 lipid A molecules per MNC). MNC-bound lipid A was confirmed by confocal microscopy after staining with antilipid A antibody (Abcam, Cambridge, MA). DCs were also stimulated with 100 ng/mL of free lipid A as a positive control.[47−49]

Cell Viability Assay. Cell viability was measured by MTT assay (Sigma). DCs (1 × 10^6 cells) were pulsed with the indicated amount of MNCs for various time periods. Then, MTT (0.5 mg/mL) was added directly to each well and incubated further for 4 h at 37 °C. To analyze the MTT reduction colorimetrically, absorbance was measured at 560 nm using a plate reader (PerkinElmer Wallace 1420 Victor) after adding dimethyl sulfoxide.

Flow Cytometric Analysis. DCs were washed with ice-cold fluorescence-activated cell sorter (FACS) buffer (PBS containing 1% bovine serum albumin (BSA) and 1 mM ethylenediaminetetraacetic acid and blocked on ice for 30 min with ultrablock solution containing 10% rat sera, 10% hamster sera, 10% mouse sera (Sigma), and 10 μg/mL of 2.4 G2 monoclonal antibody (BD Pharmingen). The cells were subsequently stained with the following antibodies: APC/Cy7-conjugated anti-CD11c (clone N418, BioLegend), PE/Cy7-conjugated anti-CD86 (clone GL-1, BioLegend), PE-conjugated anti-CD40 (clone 3/23, BD Pharmingen), APC-conjugated anti-CD80 (clone 16-10A1, eBioscience). Dead cells were excluded by staining with 7-amino-actinomycin D (7-AAD, BD Pharmingen). The cells were analyzed using a FACS Canto II flow cytometer (BD Biosciences). Data were analyzed by FlowJo software version 8.8.6 (FlowJo).

MRI. MRI images were acquired with a 9.4 T 160AS (Agilent Technologies). To determine whether DCs pulsed with MNCs could be detected by MRI, a rapid MRI examination was performed that involved a T1-weighted (T1w) spin echo sequence and a T2-weighted (T2w) rapid acquisition with relaxation enhancement (RARE) sequence. To investigate the magnetic resonance (MR) signal intensity according to the cell-labeling conditions, a T2 measurement of the labeled cells was performed. The imaging protocol for T2 measurements was based on the multi echo spin−echo pulse sequence, with imaging parameters of TR = 4000 ms; number of echo train = 52; echo spacing = 8.03 ms; 128 × 64 matrix; field of view (FOV) = 1 × 1 cm^2; slice thickness = 2 mm.

In Vivo Migration Assay of DCs. C57BL/6 mice were preinjected with lipopolysaccharide (300 ng/leg) in the hind-leg footpad at 1 day before injection of DCs. DCs (10^6 cells/ml) were stimulated with indicated agents for 18 h prior to labeling with 5-(and 6)-(((4-chloromethyl)benzoyl)amino)-tetramethylrhodamine (CMTMR) (Molecular Probes). Cells were incubated with CMTMR (10 μM) for 10 min at 37 °C, washed with PBS containing 0.5% of BSA twice, and resuspended in PBS at a concentration of 10^6 cells/ml. The cell solution (30 μL) was injected into the footpad of C57BL/6 mice. Forty-eight hours later, popliteal lymph nodes were collected and treated with 1 mg/mL of collagenase D (Sigma) for 40 min at 37 °C to collect the cells in lymph nodes. The percentage of migrated DCs in total lymph node cells was determined by FACS analysis.

Intracellular Cytokine Staining. Eight-week-old C57BL/6 mice were immunized at the tail base with DCs (2 × 10^6 cells/mouse) pulsed with cacinoembryonic antigen (CEA)-derived T cell epitopes[50,51] twice at weekly intervals. CEA-derived peptides (CEA526-533: EAQNTTYL, CEA174-189: TYLWWVNNQSLPVSP, CEA420-434: SPSYTNYYRPGVNLSL, CEA570-584: CGIQNSVSANRSOPV, CEA645-660: TPNNNGTYACFVSNL) were synthesized at

the purity of >90% (Peptron Inc.), mixed at concentration of 10 μg/mL in PBS, and used for DC pulsing. One week after the second immunization, lymphocytes were collected from the spleens or the superficial inguinal and periaortic lymph nodes, and the lymphocytes were cultured for 16 h in Roswell Park Memorial Institute (RPMI) 1640 medium supplemented with 10% heat-inactivated fetal bovine serum (FBS), 50 nM β-mercaptoethanol (Invitrogen), 100 units/ml penicillin-streptomycin, 2 mM L-glutamine (Welgene), and 20 μg/mL of CEA peptides in 24-well, flat-bottomed culture plates (5×10^6 cells/well). After incubation, GolgiPlug (BD Biosciences) was added for 4 h. Lymphocytes were washed three times with ice-cold FACS buffer. Cells were blocked with ultrablock solution for 30 min on ice and stained with fluorescein isothiocyanate (FITC)-conjugated CD4 or CD8 antibodies (BD Pharmingen) for 30 min at 4 °C. After surface CD4 or CD8 staining, cells were washed three times with ice-cold FACS buffer and subjected to intracellular cytokine staining using the Cytofix/Cytoperm kit (BD Biosciences). Intracellular interferon-γ (IFN-γ) was stained using an APC-conjugated anti-IFN-γ antibody (clone: XMG1.2; BD Pharmingen) for 30 min at 4 °C. The stained cells were analyzed with a FACS. Data were analyzed by FlowJo software version 8.8.6.

■ ASSOCIATED CONTENT

Supporting Information

Real-time movie for the collection and redispersion process of MNCs, magnetization value, magnetic separation data, cell viability test data, FACS data, TGA data, and photographs of nanoclusters, nanoparticles, and conjugated MNCs in solution. This material is available free of charge via the Internet at http://pubs.acs.org.

■ AUTHOR INFORMATION

Corresponding Authors

*E-mail: (W.K.) woongkim@korea.ac.kr.
*E-mail: (N.-H.C.) chonh@snu.ac.kr.

Author Contributions

‡J.J.and E.-K.K. contributed equally to this work.

Notes

The authors declare no competing financial interest.

■ ACKNOWLEDGMENTS

This research was supported by the Pioneer Research Center Program through the National Research Foundation of Korea (NRF-2011-0001715 and 2010-0025875) and by a Korea University Grant.

■ REFERENCES

(1) Kim, J.; Lee, J. E.; Lee, S. H.; Yu, J. H.; Lee, J. H.; Park, T. G.; Hyeon, T. Designed Fabrication of a Multifunctional Polymer Nanomedical Platform for Simultaneous Cancer- Targeted Imaging and Magnetically Guided Drug Delivery. *Adv. Mater.* **2008**, *20*, 478−483.

(2) Lee, J. E.; Lee, N.; Kim, T.; Kim, J.; Hyeon, T. Multifunctional Mesoporous Silica Nanocomposite Nanoparticles for Theranostic Applications. *Acc. Chem. Res.* **2011**, *44*, 893−902.

(3) Wang, G. N.; Su, X. G. The Synthesis and Bio-Applications of Magnetic and Fluorescent Bifunctional Composite Nanoparticles. *Analyst* **2011**, *136*, 1783−1798.

(4) Lee, D. E.; Koo, H.; Sun, I. C.; Ryu, J. H.; Kim, K.; Kwon, I. C. Multifunctional Nanoparticles for Multimodal Imaging and Theragnosis. *Chem. Soc. Rev.* **2012**, *41*, 2656−2672.

(5) Vanneman, M.; Dranoff, G. Combining Immunotherapy and Targeted Therapies in Cancer Treatment. *Nat. Rev. Cancer* **2012**, *12*, 237−251.

(6) Sabado, R. L.; Bhardwaj, N. Directing Dendritic Cell Immunotherapy towards Successful Cancer Treatment. *Immunotherapy* **2010**, *2*, 37−56.

(7) Palucka, A. K.; Ueno, H.; Fay, J. W.; Banchereau, J. Taming Cancer by Inducing Immunity via Dendritic Cells. *Immunol. Rev.* **2007**, *220*, 129−150.

(8) Melief, C. J. Cancer Immunotherapy by Dendritic Cells. *Immunity* **2008**, *29*, 372−383.

(9) Cho, N. H.; Cheong, T. C.; Min, J. H.; Wu, J. H.; Lee, S. J.; Kim, D.; Yang, J. S.; Kim, S.; Kim, Y. K.; Seong, S. Y. A Multifunctional Core−Shell Nanoparticle for Dendritic Cell-Based Cancer Immunotherapy. *Nat. Nanotechnol.* **2011**, *6*, 675−682.

(10) Palucka, K.; Banchereau, J. Cancer Immunotherapy via Dendritic Cells. *Nat. Rev. Cancer* **2012**, *12*, 265−277.

(11) Gilboa, E. DC-Based Cancer Vaccines. *J. Clin. Invest.* **2007**, *117*, 1195−1203.

(12) Lindquist, R. L.; Shakhar, G.; Dudziak, D.; Wardemann, H.; Eisenreich, T.; Dustin, M. L.; Nussenzweig, M. C. Visualizing Dendritic Cell Networks in Vivo. *Nat. Immunol.* **2004**, *5*, 1243−1250.

(13) Prince, H. M.; Wall, D. M.; Ritchie, D.; Honemann, D.; Harrrison, S.; Quach, H.; Thompson, M.; Hicks, R.; Lau, E.; Davison, J.; Loudovaris, M.; Moloney, J.; Loveland, B.; Bartholeyns, J.; Katsifis, A.; Mileshkin, L. In Vivo Tracking of Dendritic Cells in Patients with Multiple Myeloma. *J. Immunother.* **2008**, *31*, 166−179.

(14) Baumjohann, D.; Hess, A.; Budinsky, L.; Brune, K.; Schuler, G.; Lutz, M. B. In Vivo Magnetic Resonance Imaging of Dendritic Cell Migration into the Draining Lymph Nodes of Mice. *Eur. J. Immunol.* **2006**, *36*, 2544−2555.

(15) de Vries, I. J.; Lesterhuis, W. J.; Barentsz, J. O.; Verdijk, P.; van Krieken, J. H.; Boerman, O. C.; Oyen, W. J.; Bonenkamp, J. J.; Boezeman, J. B.; Adema, G. J.; Bulte, J. W.; Scheenen, T. W.; Punt, C. J.; Heerschap, A.; Figdor, C. G. Magnetic Resonance Tracking of Dendritic Cells in Melanoma Patients for Monitoring of Cellular Therapy. *Nat. Biotechnol.* **2005**, *23*, 1407−1413.

(16) Dekaban, G. A.; Snir, J.; Shrum, B.; de Chickera, S.; Willert, C.; Merrill, M.; Said, E. A.; Sekaly, R. P.; Foster, P. J.; O'Connell, P. J. Semiquantitation of Mouse Dendritic Cell Migration in Vivo Using Cellular MRI. *J. Immunother.* **2009**, *32*, 240−251.

(17) Frick, S. U.; Bacher, N.; Baier, G.; Mailander, V.; Landfester, K.; Steinbrink, K. Functionalized Polystyrene Nanoparticles Trigger Human Dendritic Cell Maturation Resulting in Enhanced CD4+T Cell Activation. *Macromol. Biosci.* **2012**, *12*, 1637−1647.

(18) Cheng, Z. L.; Al Zaki, A.; Hui, J. Z.; Muzykantov, V. R.; Tsourkas, A. Multifunctional Nanoparticles: Cost versus Benefit of Adding Targeting and Imaging Capabilities. *Science* **2012**, *338*, 903−910.

(19) Lu, Z. D.; Gao, C. B.; Zhang, Q.; Chi, M. F.; Howe, J. Y.; Yin, Y. D. Direct Assembly of Hydrophobic Nanoparticles to Multifunctional Structures. *Nano Lett.* **2011**, *11*, 3404−3412.

(20) Trinh, T. T.; Mott, D.; Thanh, N. T. K.; Maenosono, S. One-Pot Synthesis and Characterization of Well Defined Core−Shell Structure of FePt@CdSe Nanoparticles. *RSC Adv.* **2011**, *1*, 100−108.

(21) Gao, J. H.; Zhang, W.; Huang, P. B.; Zhang, B.; Zhang, X. X.; Xu, B. Intracellular Spatial Control of Fluorescent Magnetic Nanoparticles. *J. Am. Chem. Soc.* **2008**, *130*, 3710−3711.

(22) Ge, J. P.; Hu, Y. X.; Biasini, M.; Beyermann, W. P.; Yin, Y. D. Superparamagnetic Magnetite Colloidal Nanocrystal Clusters. *Angew. Chem., Int. Ed.* **2007**, *46*, 4342−4345.

(23) Cheng, C. M.; Wen, Y. H.; Xu, X. F.; Gu, H. C. Tunable Synthesis of Carboxyl-Functionalized Magnetite Nanocrystal Clusters with Uniform Size. *J. Mater. Chem.* **2009**, *19*, 8782−8788.

(24) Bae, W. K.; Kwak, J.; Park, J. W.; Char, K.; Lee, C.; Lee, S. Highly Efficient Green-Light-Emitting Diodes Based on CdSe@ZnS Quantum Dots with a Chemical-Composition Gradient. *Adv. Mater.* **2009**, *21*, 1690−1694.

(25) Zhang, W. J.; Zhang, H.; Feng, Y. Y.; Zhong, X. H. Scalable Single-Step Noninjection Synthesis of High-Quality Core/Shell Quantum Dots with Emission Tunable from Violet to Near Infrared. *ACS Nano* **2012**, *6*, 11066−11073.
(26) Smith, A. M.; Ruan, G.; Rhyner, M. N.; Nie, S. M. Engineering Luminescent Quantum Dots for in Vivo Molecular and Cellular Imaging. *Ann. Biomed. Eng.* **2006**, *34*, 3−14.
(27) Ye, M. M.; Zhang, Q.; Hu, Y. X.; Ge, J. P.; Lu, Z. D.; He, L.; Chen, Z. L.; Yin, Y. D. Magnetically Recoverable Core-Shell Nanocomposites with Enhanced Photocatalytic Activity. *Chem.—Eur. J.* **2010**, *16*, 6243−6250.
(28) Baumgartner, J.; Bertinetti, L.; Widdrat, M.; Hirt, A. M.; Faivre, D. Formation of Magnetite Nanoparticles at Low Temperature: From Superparamagnetic to Stable Single Domain Particles. *PLoS One* **2013**, *8*, e57070.
(29) Cullity, B. D.; Stock, S. R. *Elements of X-ray Diffraction*, 3rd ed; Prentice Hall: Upper Saddle River, NJ, 2001.
(30) Hermanson, G. T., *Bioconjugate Techniques*, 2nd ed; Academic Press: San Diego, 1996.
(31) Pong, B. K.; Trout, B. L.; Lee, J. Y. Modified Ligand-Exchange for Efficient Solubilization of CdSe/ZnS Quantum Dots in Water: A Procedure Guided by Computational Studies. *Langmuir* **2008**, *24*, 5270−5276.
(32) Giovanelli, E.; Muro, E.; Sitbon, G.; Hanafi, M.; Pons, T.; Dubertret, B.; Lequeux, N. Highly Enhanced Affinity of Multidentate versus Bidentate Zwitterionic Ligands for Long-Term Quantum Dot Bioimaging. *Langmuir* **2012**, *28*, 15177−15184.
(33) Bao, Y. P.; Calderon, H.; Krishnan, K. M. Synthesis and Characterization of Magnetic−Optical Co-Au Core−Shell Nanoparticles. *J. Phys. Chem. C* **2007**, *111*, 1941−1944.
(34) Wang, C.; Tian, W. D.; Ding, Y.; Ma, Y. Q.; Wang, Z. L.; Markovic, N. M.; Stamenkovic, V. R.; Daimon, H.; Sun, S. H. Rational Synthesis of Heterostructured Nanoparticles with Morphology Control. *J. Am. Chem. Soc.* **2010**, *132*, 6524−6529.
(35) Xuan, S. H.; Wang, Y. X. J.; Yu, J. C.; Leung, K. C. F. Tuning the Grain Size and Particle Size of Superparamagnetic Fe_3O_4 Microparticles. *Chem. Mater.* **2009**, *21*, 5079−5087.
(36) Ge, J. P.; Hu, Y. X.; Biasini, M.; Dong, C. L.; Guo, J. H.; Beyermann, W. P.; Yin, Y. D. One-Step Synthesis of Highly Water-Soluble Magnetite Colloidal Nanocrystals. *Chem.—Eur. J.* **2007**, *13*, 7153−7161.
(37) Hoppens, M. A.; Wheeler, Z. E. W.; Qureshi, A. T.; Hogan, K.; Wright, A.; Stanley, G. G.; Young, D.; Savage, P.; Hayes, D. Maghemite, Silver, Ceragenin Conjugate Particles for Selective Binding and Contrast of Bacteria. *J. Colloid Interface Sci.* **2014**, *413*, 167−174.
(38) Zhang, L.; He, R.; Gu, H. C. Oleic Acid Coating on the Monodisperse Magnetite Nanoparticles. *Appl. Surf. Sci.* **2006**, *253*, 2611−2617.
(39) Lan, Q.; Liu, C.; Yang, F.; Liu, S. Y.; Xu, J.; Sun, D. J. Synthesis of Bilayer Oleic Acid-Coated Fe_3O_4 Nanoparticles and Their Application in pH-Responsive Pickering Emulsions. *J. Colloid Interface Sci.* **2007**, *310*, 260−269.
(40) Coates, J. Interpretation of Infrared Spectra, A Practical Approach. *Encyclopedia of Analytical Chemistry*; John Wiley & Sons: New York, 2006.10.1002/9780470027318.a5606
(41) Sun, C.; Lee, J. S.; Zhang, M. Magnetic Nanoparticles in MR Imaging and Drug Delivery. *Adv. Drug Delivery Rev.* **2008**, *60*, 1252−1265.
(42) Moon, J. J.; Huang, B.; Irvine, D. J. Engineering Nano- and Microparticles to Tune Immunity. *Adv. Mater.* **2012**, *24*, 3724−3746.
(43) Bershteyn, A.; Hanson, M. C.; Crespo, M. P.; Moon, J. J.; Li, A. V.; Suh, H.; Irvine, D. J. Robust IgG Responses to Nanograms of Antigen Using a Biomimetic Lipid-Coated Particle Vaccine. *J. Controlled Release* **2012**, *157*, 354−365.
(44) Zhang, Z.; Tongchusak, S.; Mizukami, Y.; Kang, Y. J.; Ioji, T.; Touma, M.; Reinhold, B.; Keskin, D. B.; Reinherz, E. L.; Sasada, T. Induction of Anti-Tumor Cytotoxic T Cell Responses Through PLGA-Nanoparticle Mediated Antigen Delivery. *Biomaterials* **2011**, *32*, 3666−3678.
(45) Deng, H.; Li, X. L.; Peng, Q.; Wang, X.; Chen, J. P.; Li, Y. D. Monodisperse Magnetic Single-Crystal Ferrite Microspheres. *Angew. Chem., Int. Ed.* **2005**, *44*, 2782−2785.
(46) Wu, J. M.; Gao, L. Z.; Gao, D. Multistage Magnetic Separation of Microspheres Enabled by Temperature-Responsive Polymers. *ACS Appl. Mater. Interfaces* **2012**, *4*, 3041−3046.
(47) Park, B. S.; Song, D. H.; Kim, H. M.; Choi, B. S.; Lee, H.; Lee, J. O. The Structural Basis of Lipopolysaccharide Recognition by the TLR4-MD-2 Complex. *Nature* **2009**, *458*, 1191−1195.
(48) Kagan, J. C.; Su, T.; Horng, T.; Chow, A.; Akira, S.; Medzhitov, R. TRAM Couples Endocytosis of Toll-Like Receptor 4 to the Induction of Interferon-Beta. *Nat. Immunol.* **2008**, *9*, 361−368.
(49) Husebye, H.; Halaas, O.; Stenmark, H.; Tunheim, G.; Sandanger, O.; Bogen, B.; Brech, A.; Latz, E.; Espevik, T. Endocytic Pathways Regulate Toll-Like Receptor 4 Signaling and Link Innate and Adaptive Immunity. *EMBO J.* **2006**, *25*, 683−692.
(50) Schmitz, J.; Reali, E.; Hodge, J. W.; Patel, A.; Davis, G.; Schlom, J.; Greiner, J. W. Identification of an Interferon-Gamma-Inducible Carcinoembryonic Antigen (CEA) CD8(+) T-Cell Epitope, Which Mediates Tumor Killing in CEA Transgenic Mice. *Cancer Res.* **2002**, *62*, 5058−5064.
(51) Bos, R.; van Duikeren, S.; van Hall, T.; Kaaijk, P.; Taubert, R.; Kyewski, B.; Klein, L.; Melief, C. J.; Offringa, R. Expression of a Natural Tumor Antigen by Thymic Epithelial Cells Impairs the Tumor-Protective CD4+ T-Cell Repertoire. *Cancer Res.* **2005**, *65*, 6443−6449.